J. Fluid Mech. (2025), *vol.* 1018, A18, doi:10.1017/jfm.2025.10525

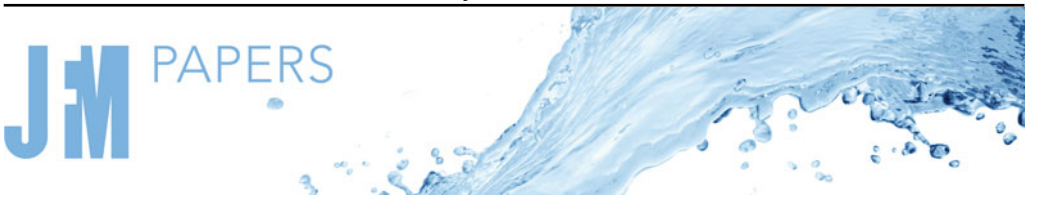

Acoustic-gravity quantum tunnelling analogy

Usama Kadri[1], **Ali Abdolali**[2,3] **and James T. Kirby**[4]

[1]School of Mathematics, Cardiff University, Cardiff CF24 4AG, UK

[2]USACE Engineer Research and Development Center, Coastal and Hydraulics Laboratory, Vicksburg, MS, USA

[3]Earth System Science Interdisciplinary Center (ESSIC), University of Maryland, College Park, MD, USA

[4]Center for Applied Coastal Research, Department of Civil, Construction and Environmental Engineering, University of Delaware, Newark DE 19716, USA

Corresponding author: Usama Kadri, usama.kadri@gmail.com

(Received 19 December 2024; revised 16 July 2025; accepted 24 July 2025)

We present a mathematical solution for the two-dimensional linear problem involving acoustic-gravity waves interacting with rectangular barriers at the bottom of a channel containing a slightly compressible fluid. Our analysis reveals that, below a certain cutoff frequency, the presence of a barrier inhibits the propagation of acoustic-gravity modes. However, through the coupling with evanescent modes existing in the barrier region, we demonstrate the phenomenon of 'tunnelling' where the incident acoustic-gravity wave energy can leak to the other side of the barrier, creating a propagating acoustic-gravity mode of the same frequency. Notably, the amplitude of the tunnelling waves exponentially decays with the width of the barrier, analogous to the behaviour observed in quantum tunnelling phenomena. Moreover, a more general solution for multi-barrier and multi-modes is discussed. It is found that tunnelling energy tends to transform from an incident mode to the lowest neighbouring modes. Resonance due to barrier length results in more efficient energy transfer between modes.

Key words: acoustics, detonation waves, geophysical and geological Flows

1. Introduction

The interaction of waves with barriers in various physical systems has been a topic of great interest and importance. Understanding the behaviour of waves when encountering obstacles allows us to analyse and predict the transmission, reflection and scattering phenomena that arise in a wide range of scenarios. In classical physics, there is a range

of implications from the scattering of surface-gravity waves due to seabed irregularities (e.g. Mei, Stiassnie & Yue 2005), to the interaction of acoustic-gravity waves with shelf breaks and trenches resembling variable depth in ocean (Kadri & Stiassnie 2012; Sammarco *et al.* 2013; Abdolali, Kirby & Bellotti 2015; Kadri 2015). Further examples are found in quantum physics, from fusion reactions in stars (Balantekin & Takigawa 1998) to miniaturisation in microchips (Kelly & Weisbuch 1986).

In this study, we focus on the interaction of acoustic-gravity waves with rectangular barriers submerged in water. Acoustic-gravity waves are a type of wave that propagates through a medium, such as water, and exhibits characteristics influenced by both gravity and compressibility effects (Abdolali, Kadri & Kirby 2019). These waves play a crucial role in various natural phenomena, including oceanic dynamics, underwater acoustics and geophysical processes.

The interaction of acoustic-gravity waves with rectangular barriers gives rise to intriguing wave phenomena, namely energy tunnelling at a large scale. By studying this interaction, we derive mathematical expressions that describe the transmission and reflection coefficients as function of the barrier length. Notably, we find that the transmission coefficient exhibits exponential decay with increasing barrier width, reminiscent of the phenomenon of quantum tunnelling encountered in particle physics.

Moreover, we study resonance effects involving multiple barriers. Resonance effects in barrier transmission typically occur in potentials with multiple peaks and a trough between them. In quantum mechanics it is well documented that the transmission probability sharply rises, reaching its peak when the kinetic energy of an incoming particle resonates with one of the quasi-bound energy levels within the trough (Child 1967; Connor 1968). This mechanism allows efficient tunnelling processes, even when the energy is significantly below the barrier's peak. A similar phenomenon is observed in the field of surface water waves, where either partial reflection or full transmission under tunnelling effects is governed by the geometry of submarine irregularities such canyons (Kirby & Dalrymple 1983; Thomson, Elgar & Herbers 2005). This effect arises from the interplay between the wave dynamics and the topography of bumps or trenches, which can either permit or block the passage of waves depending on their angle, energy and the specific features of the irregularities (Kirby & Dalrymple 1983; Thomson *et al.* 2005). Interestingly, a very similar behaviour is observed for the interaction of acoustic-gravity waves interacting with multiple barriers. The analogy between the transmission and reflection coefficients in our acoustic-gravity wave system and those encountered in quantum tunnelling provides an intriguing connection between the wave dynamics and particle behaviour.

2. Preliminaries

Consider the interaction of an incident acoustic-gravity wave disturbance in water of depth $z_0^{(0)}$ with a single rectangular barrier. The water depths at and after the barrier are $z_0^{(1)}$ and $z_0^{(2)}$, respectively – see figure 1 regions (0), (1) and (2). We choose the water depth in zone 0 as the length scale and so the normalised depth is $z_0^{(0)} = 1$, and $z_0^{(0)}/c$ is the time scale, where c is the speed of sound in water and α is the mode amplitude. We also introduce a small non-dimensional parameter $\mu = g z_0^{(0)}/c^2$, which governs the effects of gravity (g is the gravitational constant) relative to compressibility. Assuming an irrotational flow, the wave problem is formulated in terms of the two-dimensional velocity potential $\varphi(x, z, t)$, where $\boldsymbol{u} = \boldsymbol{\nabla}\varphi$ is the velocity field. By neglecting nonlinear terms, the equation governing φ in the fluid interior is obtained by combining continuity with the unsteady Bernoulli equation (see Bondi 1947)

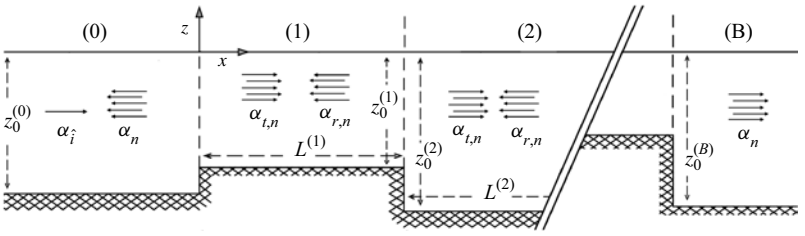

Figure 1. Definition sketch of multiple steps.

$$\varphi_{tt} - (\varphi_{xx} + \varphi_{zz}) + \mu\varphi_z = 0, \quad -z_0 < z < 0. \tag{2.1}$$

The bottom boundary condition is considered rigid, implying

$$\varphi_z = 0, \quad z = -z_0^{(j)}, \quad j = 0, 1, 2, \ldots. \tag{2.2}$$

Here, $z_0^{(j)}$ is normalised by $z_0^{(0)}$. On the other hand, at the free surface, the combined kinematic and dynamic boundary condition requires that

$$\varphi_{tt} + \mu\varphi_z = 0, \quad z = 0. \tag{2.3}$$

Note that variations in the speed of sound can reach a maximum of $O(\mu)$, as shown by Michele & Renzi (2020). However, these become more relevant when considering acoustic modes with length scales much smaller than z_0. For long-wavelength waves, however, the entire water column effectively acts as a waveguide, allowing any minor variations in sound speed to be averaged out, making the detailed sound speed profile effectively negligible for the problem addressed here.

Conversely, elasticity effects become important for acoustic-gravity waves propagating at near-critical depths (Eyov *et al.* 2013). To avoid unnecessary inclusion of elasticity, we treat the physical problem as follows: an incident acoustic-gravity mode can be divided into two parts. The first part reflects and penetrates through the elastic barrier, while the second part reflects and transitions into acoustic modes (evanescent and higher progressive modes where applicable) within the barrier zone. Since our focus is on tunnelling effects, this study explicitly concerns the second part. The effect of elasticity are revisited in the conclusion section.

2.1. *Solution*

The fundamental solution in a domain with constant depth is obtained by employing the separation of variables for the potential φ, yielding

$$\varphi = \alpha_n f_n(z) \exp\left(\frac{1}{2}\mu z\right) \exp\{\mathrm{i}(k_n x - \omega t)\}, \quad n = 0, 1, 2, \ldots, \tag{2.4}$$

where α_n represents the amplitude of the nth mode, k_n is the wavenumber of the nth mode, and ω is the frequency. To leading order, neglecting terms $O(\mu^2)$, the system of partial differential equations reduces to a set of ordinary differential equations (the index j was omitted unless necessary)

$$f_{zz} + \Omega^2 f = 0, \quad -z_0 < z < 0, \tag{2.5}$$

$$f_z + \frac{1}{2}\mu f = 0, \quad z = -z_0, \tag{2.6}$$

$$\mu f_z - \omega^2 f = 0, \quad z = 0, \tag{2.7}$$

and the solution of the orthonormal eigenfunctions given by

$$f(z) = \frac{\cos \Omega(z + z_0)}{\sqrt{I}}, \tag{2.8}$$

$$I = \int_{-z_0}^{0} \cos^2 \Omega(z + z_0) \mathrm{d}z = \frac{2\Omega z_0 + \sin(2\Omega z_0)}{4\Omega}, \tag{2.9}$$

where Ω is the eigenvalue satisfying

$$\Omega^2 = \omega^2 - k^2. \tag{2.10}$$

Substituting (2.4) into (2.5)–(2.7) yields the dispersion relation

$$\omega^2 = -\mu \frac{\Omega^2 - k^2}{2\Omega} \tan(\Omega z_0) + O(\mu^2). \tag{2.11}$$

Substituting into the dispersion relation and making use of trigonometric identities gives

$$\omega^2 = k^2 + \omega_n^2 - \mu \frac{k^2 - \omega_n^2}{k^2 + \omega_n^2} + O(\mu^2), \quad n = 1, 2, 3 \ldots, \tag{2.12}$$

where $\omega_n = (n - 1/2)\pi$. Noting that for progressive acoustic-gravity waves Ω and k are real.

It is noteworthy that when $\omega > \Omega$, k is real, and the dispersion relation corresponds to progressive modes. Conversely, when $\omega < \Omega$, $k = \mathrm{i}\kappa$ is purely imaginary, and the same dispersion relation corresponds to evanescent modes.

Note that, if the contribution of the gravity wave is considered, then the water depth should not be assumed deep. Under that setting, $\Omega \simeq \mathrm{i}k$, the well-known dispersion relation for the gravity waves can be directly derived from (2.11)

$$\omega^2 = \mu k \tanh(k z_0). \tag{2.13}$$

Under this setting, we shall refer to the gravity mode as the zeroth mode, $n = 0$.

3. Interaction with a barrier

The solution at the left side of the barrier, denoted by (0), consists of an incident mode $\hat{i}$ with amplitude $\alpha_{\hat{i}}$, and an infinite sum of reflected modes

$$\Phi^{(0)} = \alpha_{\hat{i}}^{(0)} \frac{\cos \Omega_n^{(0)}\left(z + z_0^{(0)}\right)}{\sqrt{I_n^{(0)}}} \mathrm{e}^{\mathrm{i}\left(k_{\hat{i}}^{(0)} x - \omega t\right)} + \sum_{n=0}^{\infty} \left(\alpha_n^{(0)} \frac{\cos \Omega_n^{(0)}\left(z + z_0^{(0)}\right)}{\sqrt{I_n^{(0)}}} \mathrm{e}^{-\mathrm{i}\left(k_n^{(0)} x + \omega t\right)} \right). \tag{3.1}$$

Here, and in what follows superscript (j), with $j = 0, 1, 2, \ldots$ denote the different regions defined in figure 1, subscripts $\hat{i}$ and n represent the incident and reflected modes, respectively. In the barrier zone (1)

$$\Phi^{(1)} = \sum_{n=0}^{\infty} \frac{\cos \Omega_n^{(1)}\left(z + z_0^{(1)}\right)}{\sqrt{I_n^{(1)}}} \left(\alpha_{t,n}^{(1)} \mathrm{e}^{\mathrm{i}\left(k_n^{(1)} x - \omega t\right)} + \alpha_{r,n}^{(1)} \mathrm{e}^{-\mathrm{i}\left(k_n^{(1)} x + \omega t\right)} \right), \tag{3.2}$$

where subscripts t, n and r, n represent the transmitted and reflected nth modes, respectively. At the right side of the barrier (2), there is an infinite sum of transmitted modes

$$\Phi^{(2)} = \sum_{n=0}^{\infty} \left(\alpha_n^{(2)} \frac{\cos \Omega_n^{(2)} \left(z + z_0^{(2)}\right)}{\sqrt{I_n^{(2)}}} \mathrm{e}^{-\mathrm{i}\left(k_n^{(2)} x + \omega t\right)} \right). \tag{3.3}$$

Matching $\Phi^{(0)} = \Phi^{(1)}$ at $x = 0$ gives

$$\alpha_{\hat{i}}^{(0)} \mathcal{J}_{\hat{i}M} + \sum_{n=0}^{\infty} \left(\alpha_{r,n}^{(0)} \mathcal{J}_{nM}^{(0)} \right) = \alpha_{t,M}^{(1)} + \alpha_{r,M}^{(1)}, \quad M = 0, 1, 2, \ldots. \tag{3.4}$$

Similarly, matching $\Phi^{(1)} = \Phi^{(2)}$ at $x = L$ gives

$$\sum_{n=0}^{\infty} \mathcal{J}_{Mn} \left(\alpha_{t,n}^{(1)} \mathrm{e}^{\mathrm{i}k_n^{(1)} L} + \alpha_{r,n}^{(1)} \mathrm{e}^{-\mathrm{i}k_n^{(1)} L} \right) = \alpha_{t,M}^{(2)} \mathrm{e}^{\mathrm{i}k_n^{(2)} L}, \quad M = 0, 1, 2, \ldots. \tag{3.5}$$

Finally, matching the horizontal velocity at $x = 0$ and $x = L$ gives the two conditions

$$\mathrm{i}k_{\hat{i}} \alpha_{\hat{i}}^{(0)} \delta_{\hat{i}M} - \mathrm{i}k_M^{(0)} \alpha_{r,M}^{(0)} = \sum_{m=0}^{\infty} \mathrm{i}k_m \mathcal{J}_{Mm} \left(\alpha_{t,m}^{(1)} - \alpha_{r,m}^{(1)} \right), \quad M = 0, 1, 2, \ldots, \tag{3.6}$$

$$\mathrm{i}k_M \left(\alpha_{t,m}^{(1)} \mathrm{e}^{\mathrm{i}k_M^{(1)} L} - \alpha_{r,m}^{(1)} \mathrm{e}^{-\mathrm{i}k_M^{(1)} L} \right) = \sum_{m=0}^{\infty} \mathrm{i}k_m^{(2)} \alpha_{t,m}^{(2)} \mathcal{J}_{Mm} \mathrm{e}^{\mathrm{i}k_m^{(2)} L}, \quad M = 0, 1, 2, \ldots. \tag{3.7}$$

Here, $\delta_{\hat{i}M}$ is the Kronecker delta and the integral $\mathcal{J}_{nm}$ between two regions l and $l+1$ where $l = [0, 1]$ is defined as

$$\mathcal{J}_{nm} = \int_{-z_0^{(j)}}^{0} \frac{\cos \Omega_n^{(l)} \left(z + z_0^{(l)}\right) \cos \Omega_m^{(l+1)} \left(z + z_0^{(l+1)}\right)}{\sqrt{I_n^{(l)} I_m^{(l+1)}}} \mathrm{d}z, \quad j = l, l+1, \tag{3.8}$$

$$\begin{aligned} \mathcal{J}_{nm} = {} & \left(I_n^{(l)} I_m^{(l+1)}\right)^{-1/2} \left(\Omega_m^{(l+1)^2} - \Omega_n^{(l)^2}\right)^{-1} \left[\Omega_m^{(l+1)} \cos\left(\Omega_n^{(l)} z_0^{(l)}\right) \sin\left(\Omega_m^{(l+1)} z_0^{(l+1)}\right)\right. \\ & \left. - \Omega_{l_j}^{(j)} \sin\left(\Omega_{l_j}^{(j)} \left(z_0^{(l+1)} - z_0^{(l)}\right)\right) - \Omega_n^{(l)} \cos\left(\Omega_m^{(l+1)} z_0^{(l+1)}\right) \sin\left(\Omega_n^{(l)} z_0^{(l)}\right)\right], \\ l_j = {} & \begin{cases} n, & \text{if } j = l; \\ m, & \text{if } j = l+1. \end{cases} \end{aligned} \tag{3.9}$$

By applying the boundary condition equilibrium at the interfaces between regions $b = 0, 1, \ldots, B$ and for modes $n = 0, 1, \ldots, N$, ensuring continuity of both the potential (3.4)–(3.5) and velocity (3.6)–(3.7), a linear system of equations is constructed. This system can be represented by a square matrix of size $[2B \times (N+1)] \times [2B \times (N+1)]$, corresponding to $N+1$ modes across B interfaces. In the case of a single barrier ($B = 2$), the matrix has dimensions $4(N+1) \times 4(N+1)$. The matrix size increases accordingly for multi-barrier cases discussed in the following sections. Solving this system yields an equal number of unknown reflection and transmission coefficients, $\alpha_{r,n}^{(b)}$ and $\alpha_{t,n}^{(b)}$, respectively.

These conditions and expressions govern the interaction of the acoustic-gravity waves and the surface-gravity wave with the barrier and allow us to determine the amplitudes of the reflected and transmitted modes for a given incident mode. The transmission coefficient is maximal when the total number of modes allowed in each region is one, i.e. evanescent in the barrier zone and progressive elsewhere, as shown in figure 2.

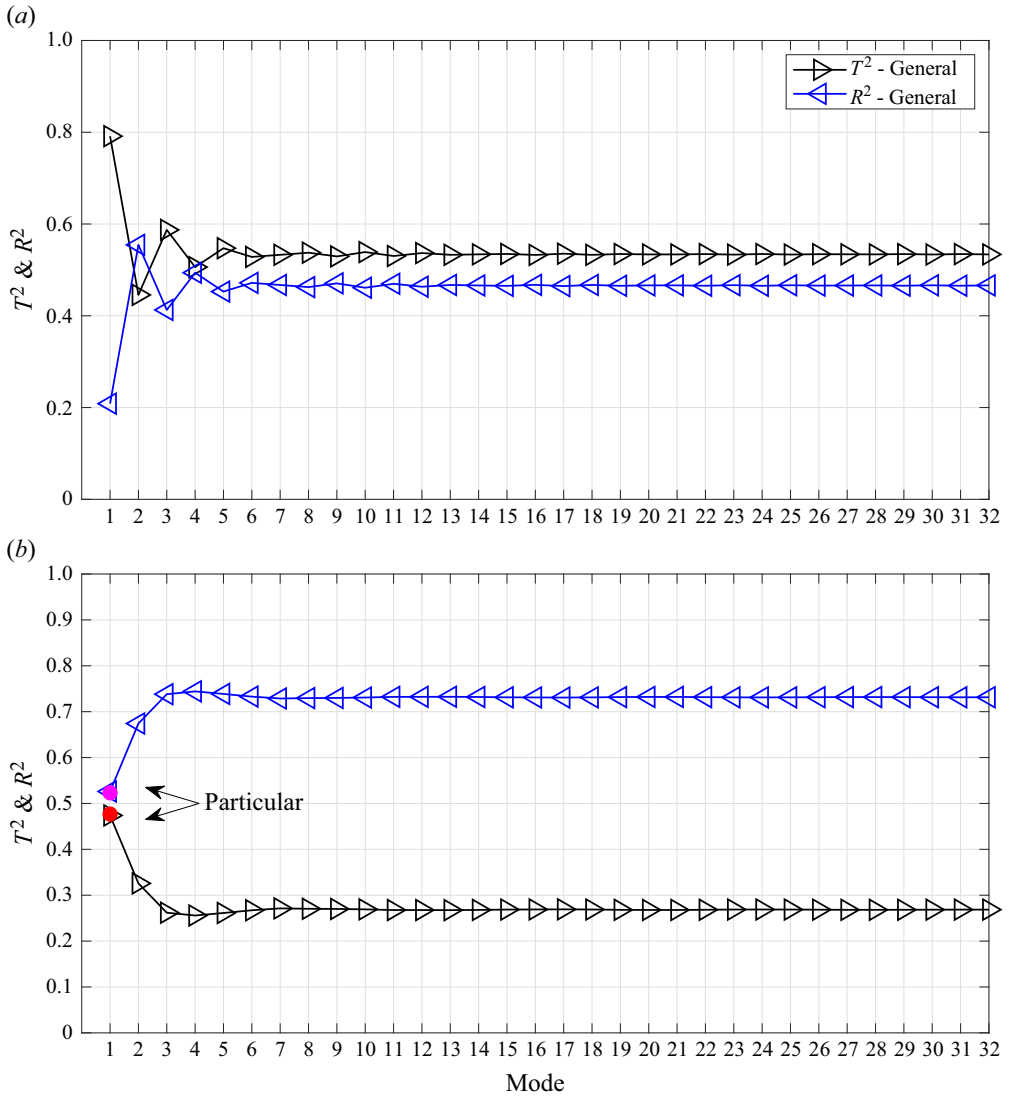

Figure 2. General solution convergence for (*a*) surface-gravity wave as the incident wave with $\lambda/z_0^{(0)} = 16$ and (*b*) acoustic–gravity wave as the incident wave with $\lambda/z_0^{(0)} = 12.5$; in both cases, $L/z_0^{(0)} = 0.5$ and $z_0^{(1)}/z_0^{(0)} = 0.75$.

The more modes that are allowed before the barrier, the more energy is reflected through mode conversion, leaving less energy available for transfer into evanescent modes, and thus reducing tunnelling. This scenario is referred to as a particular solution. When allowing more evanescent modes, energy transfer by the higher modes is less efficient and therefore the total transmission reduces almost by a factor of two. On the other hand, increasing the number of modes beyond 25 has a negligible impact on the transmitted modes, as the relative difference falls below 1 % and the higher-order modes contribute very little to energy transfer (see figure 4 of Kadri & Stiassnie (2012)). Note that, to ensure convergence of the solution, including a sufficiently large number of evanescent modes is necessary.

3.1. *Particular solution*

Consider the scenario where only a single incident mode is allowed, specifically the first acoustic-gravity mode, which propagates from left to right and interacts with the rectangular barrier. We will assume that the water depth in zones 0 and 2 is just above the cutoff frequency, i.e. deep enough to allow the first acoustic-gravity wave to be progressive, while in region 1 it is just below the cutoff frequency, allowing only evanescent modes to exist. This can be expressed as $z_0^{(0)} = z_0^{(2)} = z_0^{(1)} + \Delta z$, where $\Delta z \ll 1$. With this set-up, the conditions between the zones can be reduced to the following expressions:

$$\alpha_i^{(0)} \tilde{f}^{(0)} + \alpha_r^{(0)} \tilde{f}^{(0)} = \alpha_t^{(1)} \tilde{f}^{(1)} + \alpha_r^{(1)} \tilde{f}^{(1)}, \tag{3.10}$$

$$\alpha_t^{(1)} \tilde{f}^{(1)} \mathrm{e}^{-\kappa L} + \alpha_r^{(1)} \tilde{f}^{(1)} \mathrm{e}^{+\kappa L} = \alpha_t^{(2)} \tilde{f}^{(2)} \mathrm{e}^{\mathrm{i}kL}, \tag{3.11}$$

and two equations for their derivatives

$$\mathrm{i}k\alpha_i^{(0)} \tilde{f}^{(0)} - \mathrm{i}k\alpha_r^{(0)} \tilde{f}^{(0)} = -\kappa\alpha_t^{(1)} f^{(1)} + \kappa\alpha_r^{(1)} \tilde{f}^{(1)}, \tag{3.12}$$

$$-\kappa\alpha_t^{(1)} \tilde{f}^{(1)} \mathrm{e}^{-\kappa L} + \kappa\alpha_r^{(1)} \tilde{f}^{(1)} \mathrm{e}^{+\kappa L} = \mathrm{i}k\alpha_t^{(2)} \tilde{f}^{(2)} \mathrm{e}^{\mathrm{i}kL}. \tag{3.13}$$

After simplification, these equations lead to

$$T^2 = \frac{|\alpha_t^{(2)}|^2}{|\alpha_i^{(0)}|^2} = \frac{\left(\tilde{f}^{(0)}/\tilde{f}^{(2)}\right)^2}{1 + \Gamma^2 \sinh^2(\kappa L)}, \tag{3.14}$$

where

$$\Gamma = \frac{k^2 + \kappa^2}{2k\kappa}. \tag{3.15}$$

Similarly, the reflection coefficient can be expressed as

$$R^2 = \frac{1 - \tilde{f}^{(0)}/\tilde{f}^{(2)} + \Gamma^2 \sinh^2(\kappa L)}{1 + \Gamma^2 \sinh^2(\kappa L)}. \tag{3.16}$$

If we assume that $f^{(0)} = f^{(2)}$, the transmission and reflection coefficients can be further simplified

$$T^2 = \frac{1}{1 + \Gamma^2 \sinh^2(\kappa L)}; \quad R^2 = \frac{\Gamma^2 \sinh^2(\kappa L)}{1 + \Gamma^2 \sinh^2(\kappa L)}. \tag{3.17}$$

The particular solution result is in agreement with the general single-barrier result, presented in figure 2(*b*) with circles in the case of a single mode, i.e. the particular solution. The result here is equivalent to the result for scattering of obliquely incident surface-gravity waves from a deep trench, described by Kirby & Dalrymple (1983), (4.4). In the limit where $\kappa L \gg 1$, the transmission coefficient can be approximated as

$$T = \frac{2}{\Gamma} \mathrm{e}^{-\kappa L}. \tag{3.18}$$

This implies that the transmission decays exponentially with increasing barrier width, resembling the phenomenon of quantum tunnelling. It is interesting to note the similarity between the transmission and reflection coefficients in this system and those encountered in quantum tunnelling. In quantum mechanics, the coefficients are given by

$$\kappa^2 = \frac{2m(V - E)}{\hbar^2}; \quad k^2 = -\frac{2mE}{\hbar}. \tag{3.19}$$

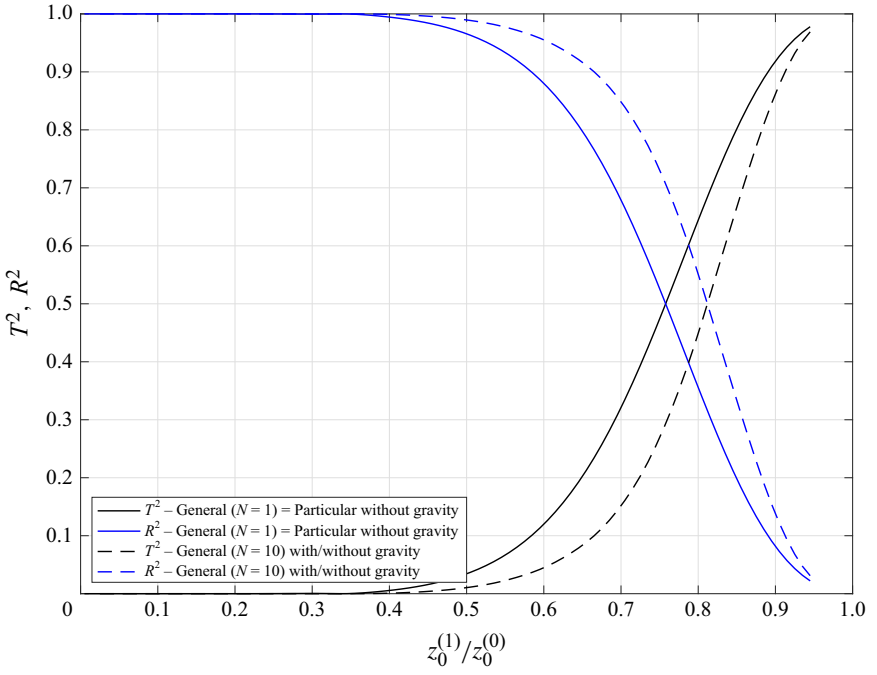

Figure 3. General solution for $\lambda/z_0^{(0)} = 12.5$ and $L/z_0^{(0)} = 0.5$. Solid curves: general solution computed using a single mode without gravity, coinciding with the particular solution. Dashed curves: general solution using 32 modes, with and without gravity mode.

Here, m represents the mass of the particle, E is the particle energy, V is the potential energy of the barrier and $\hbar$ is Planck's constant. The analogy suggests that there are underlying similarities between the behaviour of waves and particles in certain physical systems. Thus, the transmission and reflection coefficients in (3.1) behave exactly as in the quantum tunnelling of a single potential barrier, as shown in figure 3. However, in the general case with 32 modes (with and without gravity) a smaller potential is required to achieve a similar energy transmission, thus tunnelling becomes less efficient. Interestingly, for an incident acoustic mode, the contribution of the gravity mode, which is always progressive, becomes negligible as the acoustic mode approaches its critical value. Within the frequency range of this study, the gravity mode lies in the deep-water limit, where surface-gravity waves do not interact with the barrier. The critical value corresponds to the rightmost end of the curves in the figure. It is worth noting that gravity waves may still form when two progressive acoustic-gravity wave modes propagate simultaneously. However, this results from nonlinear triad resonance (see Zuccoli & Kadri 2025 for details), which lies beyond the scope of this work.

3.2. *Gravity as an incident mode*

Consider the scenario where the gravity mode ($n = 0$) serves as the incident wave. In this case, the associated eigenvalue Ω_0 is purely imaginary, while the corresponding wavenumber k_0 remains real across all regions. This indicates that the wave does not exhibit exponential decay within the barrier, rendering the analogy to quantum tunnelling, where energy decays exponentially with barrier length, inapplicable. Nonetheless, we focus on the scenario where all acoustic modes ($n \geqslant 1$) are assumed to be evanescent, allowing energy leakage through these modes.

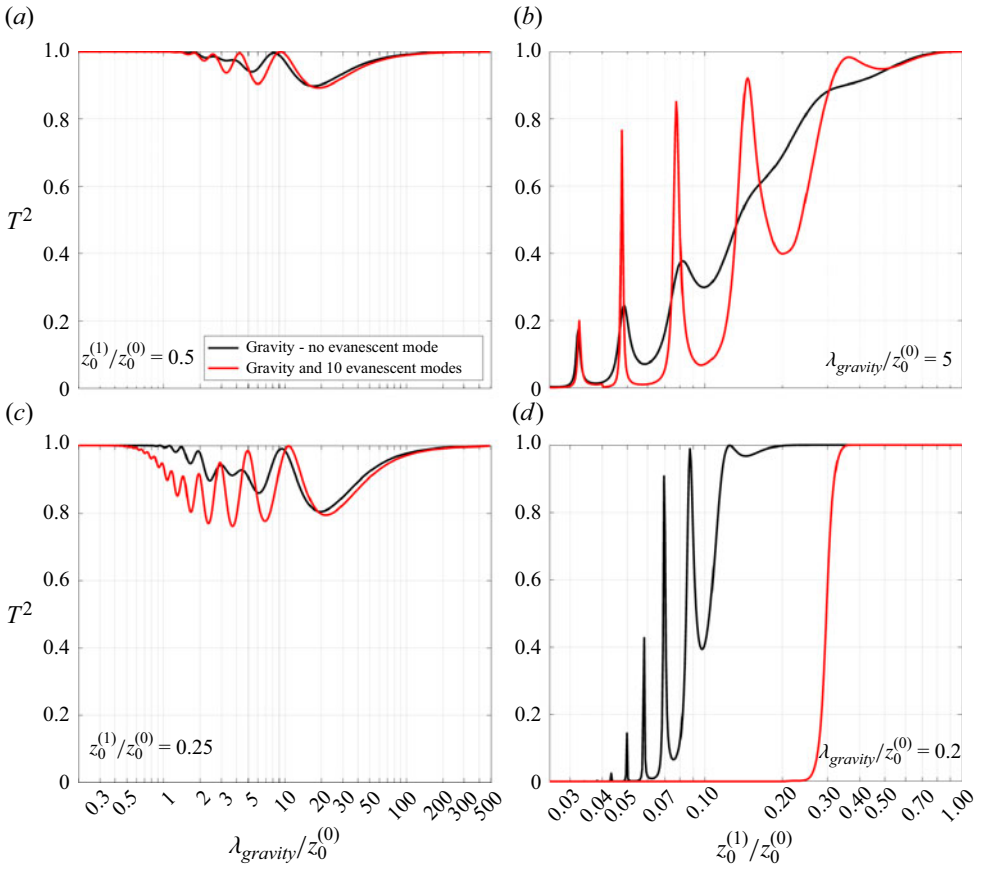

Figure 4. Transmission coefficient of an incident gravity wave as a function of wavelength, $\lambda_{gravity}/z_0^{(0)}$ (left panels), and barrier depth, $z_0^{(1)}/z_0^{(0)}$ (right panels), for a fixed barrier length of $L/z_0^{(0)} = 3$. Panels (*a*) and (*b*) depict variations with wavelength at fixed barrier depths of $z_0^{(1)}/z_0^{(0)} = 0.5$ and 0.25, respectively. Panels (*c*) and (*d*) illustrate variations with barrier depth at fixed wavelengths of $\lambda_{gravity}/z_0^{(0)} = 3$ and 0.2, respectively. The black curves represent the solution with a single propagating gravity mode, excluding evanescent modes. The red curves indicate the converged general solution, comprising one propagating gravity mode and ten evanescent acoustic modes.

In deep-water environments (corresponding to the left end of the curves in figures 4*a* and 4*b*) or when the water depth over the barrier is comparable to the depth outside it (as shown in panels *c* and *d*), the transmission coefficient tends toward one. This indicates that the gravity wave propagates through the barrier with minimal attenuation, resulting in nearly complete transmission, as expected.

In the limit of very shallow water, corresponding to the right end of the curves in panels (*a*) and (*b*) of figure 4, the barrier's influence becomes negligible, provided it does not obstruct the entire water column. In this regime, the transmission coefficient approaches unity, indicating nearly complete wave transmission. Conversely, in the deep-water limit (left end of the same panels) or when the water depth over the barrier closely matches the surrounding depth (as shown in panels *c* and *d*), the transmission coefficient also tends toward unity, especially when only the gravity mode is considered and acoustic modes are neglected, such as in an incompressible setting.

Between these two extremes, transmission is highly sensitive to the wavelength relative to the barrier length. Introducing evanescent acoustic modes ($n \geqslant 1$) leads to a noticeable decrease in the transmission coefficient compared with the incompressible case without these modes. Notably, the inclusion of evanescent modes results in a more rapid reduction of the transmission coefficient as the barrier height increases, surpassing the attenuation observed with gravity modes alone. This behaviour highlights the significant role of evanescent modes in energy leakage and wave attenuation across the barrier.

4. Interaction with multiple barriers

Consider multiple rectangular barriers with regions denoted by $b = 0, 1, 2, \ldots, B$, from left to right. The origin is located between regions (0) and (1). The distance of the left side of the bth region is x_b, e.g. $x_0 = 0$ (see figure 1). In each region the velocity potential can be written as

$$\Phi^{(b)} = \sum_{n=0}^{\infty} \frac{\cos \Omega_n^{(b)}\left(z + z_0^{(b)}\right)}{\sqrt{I_n^{(b)}}} \left(\alpha_{t,n}^{(b)} \mathrm{e}^{\mathrm{i}\left(k_n^{(b)} x - \omega t\right)} + \alpha_{r,n}^{(b)} \mathrm{e}^{-\mathrm{i}\left(k_n^{(b)} x + \omega t\right)}\right), \tag{4.1}$$

where for $b = 0$, $\alpha_{t,n}^{(0)} = 0$ for all n apart from the incident mode $n = \hat{\imath}$, and thus $\alpha_{t,\hat{\imath}}^{(0)} \equiv \alpha_{\hat{\imath}}^{(0)} \neq 0$; and for $b = B$ there are no reflected modes, i.e. $\alpha_{r,n}^{(B)} \equiv 0$. Matching $\Phi^{(b)} = \Phi^{(b+1)}$ at $x = b$ gives

$$\sum_{n=0}^{\infty} \mathcal{J}_{Mn} \left(\alpha_{t,n}^{(b)} \mathrm{e}^{\mathrm{i}k_n^{(b)} x_b} + \alpha_{r,n}^{(b)} \mathrm{e}^{-\mathrm{i}k_n^{(b)} x_b}\right) = \alpha_{t,M}^{(b+1)} \mathrm{e}^{\mathrm{i}k_n^{(b+1)} x_b} + \alpha_{r,M}^{(b+1)} \mathrm{e}^{-\mathrm{i}k_n^{(b+1)} x_b}, \quad M = 0, 1, 2, \ldots \tag{4.2}$$

Finally, matching the horizontal velocity at $x = x_b$, for $b = 0, 1, 2, \ldots, (B-1)$

$$\mathrm{i}k_M \left(\alpha_{t,m}^{(b)} \mathrm{e}^{\mathrm{i}k_M^{(b)} x_b} - \alpha_{r,m}^{(b)} \mathrm{e}^{-\mathrm{i}k_M^{(b)} x_b}\right) = \sum_{m=0}^{\infty} \mathrm{i}k_m \mathcal{J}_{Mm} \left(\alpha_{t,m}^{(b+1)} \mathrm{e}^{\mathrm{i}k_m^{(b+1)} x_b} - \alpha_{r,m}^{(b+1)} \mathrm{e}^{-\mathrm{i}k_m^{(b+1)} x_b}\right). \tag{4.3}$$

Here, the integral $\mathcal{J}_{nm}$ between two regions b and $b+1$ is defined as

$$\mathcal{J}_{nm} = \int_{-z_0^{(j)}}^{0} \frac{\cos \Omega_n^{(b)}\left(z + z_0^{(b)}\right) \cos \Omega_m^{(b+1)}\left(z + z_0^{(b+1)}\right)}{\sqrt{I_n^{(b)} I_m^{(b+1)}}} \mathrm{d}z, \quad j = b, b+1, \tag{4.4}$$

$$\begin{aligned} \mathcal{J}_{nm} = {} & \left(I_n^{(b)} I_m^{(b+1)}\right)^{-1/2} \left(\Omega_m^{(b+1)^2} - \Omega_n^{(b)^2}\right)^{-1} \Big[\Omega_m^{(b+1)} \cos\left(\Omega_n^{(b)} z_0^{(b)}\right) \sin\left(\Omega_m^{(b+1)} z_0^{(b+1)}\right) \\ & - \Omega_{l_j}^{(j)} \sin\left(\Omega_{l_j}^{(j)}\left(z_0^{(b+1)} - z_0^{(b)}\right)\right) - \Omega_n^{(b)} \cos\left(\Omega_m^{(b+1)} z_0^{(b+1)}\right) \sin\left(\Omega_n^{(b)} z_0^{(b)}\right)\Big], \\ l_j = {} & \begin{cases} n, & \text{if } j = b; \\ m, & \text{if } j = b+1. \end{cases} \end{aligned} \tag{4.5}$$

These conditions and expressions govern the interaction of the acoustic-gravity waves with the barrier and allow us to determine the amplitudes of the reflected and transmitted modes, as well as the reflection and transmission coefficients. In the following section we focus on a symmetric double barrier and derive the expressions analytically.

4.1. *Interaction with a symmetric double barrier (particular solution)*

Now consider a double barrier with its centre located at $x = 0$, with L being the length of each barrier, and d is the separation distance. Again, we assume critical conditions, $z_0^{(0)} = z_0^{(1)} - \Delta z = z_0^{(2)} = z_0^{(3)} - \Delta z = z_0^{(4)}$, allowing the propagation of a single progressive mode at the trough sides of the barriers, and a single evanescent mode at the barriers' zones. The governing equations become

$$\left(\mathrm{e}^{-\mathrm{i}k(L+d/2)} + \alpha_r^{(0)}\mathrm{e}^{\mathrm{i}k(L+d/2)}\right) f = \left(\alpha_t^{(1)}\mathrm{e}^{\kappa(L+d/2)} + \alpha_r^{(1)}\mathrm{e}^{-\kappa(L+d/2)}\right) f', \tag{4.6}$$

$$\left(\alpha_t^{(1)}\mathrm{e}^{\kappa d/2} + \alpha_r^{(1)}\mathrm{e}^{-\kappa d/2}\right) f' = \left(\alpha_t^{(2)}\mathrm{e}^{-\mathrm{i}kd/2} + \alpha_r^{(2)}\mathrm{e}^{\mathrm{i}kd/2}\right) f, \tag{4.7}$$

$$\left(\alpha_t^{(2)}\mathrm{e}^{\mathrm{i}kd/2} + \alpha_r^{(2)}\mathrm{e}^{-\mathrm{i}kd/2}\right) f = \left(\alpha_t^{(3)}\mathrm{e}^{-\kappa d/2} + \alpha_r^{(3)}\mathrm{e}^{\kappa d/2}\right) f', \tag{4.8}$$

$$\left(\alpha_t^{(3)}\mathrm{e}^{-\kappa(L+d/2)} + \alpha_r^{(3)}\mathrm{e}^{\kappa(L+d/2)}\right) f' = \alpha_t^{(4)}\mathrm{e}^{\mathrm{i}k(L+d/2)} f, \tag{4.9}$$

and the derivatives give

$$\mathrm{i}k\left(\mathrm{e}^{-\mathrm{i}k(L+d/2)} - \alpha_r^{(0)}\mathrm{e}^{\mathrm{i}k(L+d/2)}\right) f = -\kappa\left(\alpha_t^{(1)}\mathrm{e}^{\kappa(L+d/2)} - \alpha_r^{(1)}\mathrm{e}^{-\kappa(L+d/2)}\right) f', \tag{4.10}$$

$$-\kappa\left(\alpha_t^{(1)}\mathrm{e}^{\kappa d/2} - \alpha_r^{(1)}\mathrm{e}^{-\kappa d/2}\right) f' = \mathrm{i}k\left(\alpha_t^{(2)}\mathrm{e}^{-\mathrm{i}kd/2} - \alpha_r^{(2)}\mathrm{e}^{\mathrm{i}kd/2}\right) f, \tag{4.11}$$

$$\mathrm{i}k\left(\alpha_t^{(2)}\mathrm{e}^{\mathrm{i}kd/2} - \alpha_r^{(2)}\mathrm{e}^{-\mathrm{i}kd/2}\right) f = -\kappa\left(\alpha_t^{(3)}\mathrm{e}^{-\kappa d/2} - \alpha_r^{(3)}\mathrm{e}^{\kappa d/2}\right) f', \tag{4.12}$$

$$-\kappa\left(\alpha_t^{(3)}\mathrm{e}^{-\kappa(L+d/2)} - \alpha_r^{(3)}\mathrm{e}^{\kappa(L+d/2)}\right) f' = \mathrm{i}k\alpha_t^{(4)}\mathrm{e}^{\mathrm{i}k(L+d/2)} f. \tag{4.13}$$

Solving the set of equations yields

$$T = \frac{-\mathrm{e}^{-\mathrm{i}k(2L+d)}}{[\tilde{\Gamma}\sinh(2\kappa L) - 2\mathrm{i}\tilde{\Gamma}^2\sinh(\kappa L)^2]\sin(kd) - [\cosh(2\kappa L) - \mathrm{i}k\kappa\tilde{\Gamma}\sinh(2\kappa L)]\cos(kd))}, \tag{4.14}$$

$$R = \frac{\mathrm{i}\Gamma\mathrm{e}^{\mathrm{i}k(2L+d)}[-\cos(kd)\sinh(2\kappa L) + \tilde{\Gamma}\sin(kd)\cosh(2\kappa L) - \tilde{\Gamma}\sin(kd)]}{[\tilde{\Gamma}\sinh(2\kappa L) - 2\mathrm{i}\tilde{\Gamma}^2\sinh(\kappa L)^2]\sin(kd) - [\cosh(2\kappa L) - \mathrm{i}k\kappa\tilde{\Gamma}\sinh(2\kappa L)]\cos(kd))}. \tag{4.15}$$

where $\tilde{\Gamma} = (k^2 - \kappa^2)/2k\kappa$. It is easy to show that, when $d = 0$, and taking the length of each barrier $L/2$, that the single-barrier equations are retrieved. Strekalov (2018) demonstrated the significance of double-barrier phenomena and perfect transmission (i.e. no reflection) even at zero kinetic energy, once the inter-barrier distance meets a resonance criterion. Again, we see a similar analogy to quantum tunnelling even though our analytical approach is different that presented by Strekalov (2018). Analogically, perfect transmission is obtained at specific distances for a given incident mode of fixed wavenumber, as shown in figure 5; or at specific wavenumbers for given distances, as shown in figure 6. Moreover, figure 7 demonstrates the dependence of the position of resonance of k^2 on distance d, in an analogy to the dependence of the position of resonance of energy on the distance as shown in figure 2 of Strekalov (2018). In all calculations, κ was considered slightly larger than k to satisfy the critical condition discussed above. Obviously, as k^2 increases, the wave frequency increases, wavelength reduces and a smaller distance is required for the resonance conditions to be satisfied. On the other hand, the following resonance peaks are associated with the higher modes, i.e. increased k^2. Moreover, it seems that each localised resonance peak splits into multiple peaks around the original localised peak. The number of the localised peaks is equal to the number of separators, i.e. $(B/2 - 1)$,

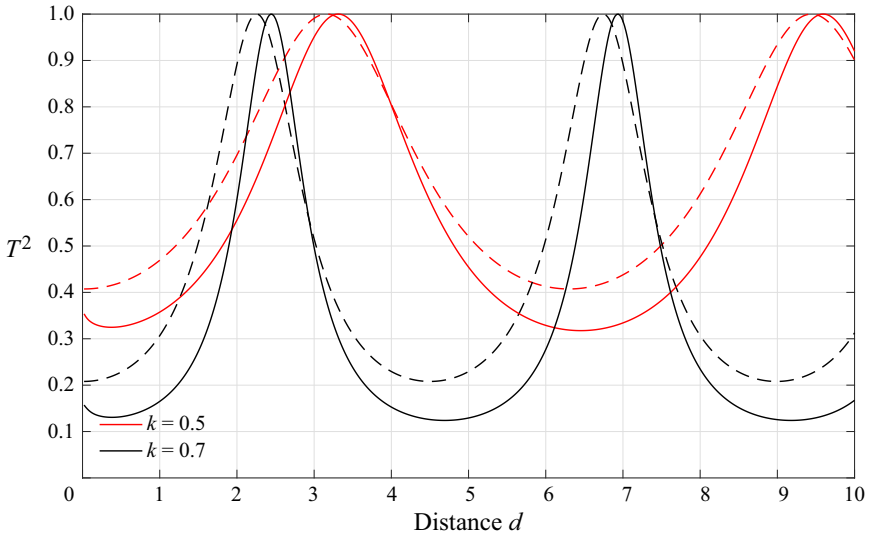

Figure 5. Transmission coefficient as a function of distance d at a fixed incident mode of wavenumber k and $L = 1$. The dashed lines represent particular solution and general solution for the case of $N = 1$. Solid lines show general solution with $N = 32$.

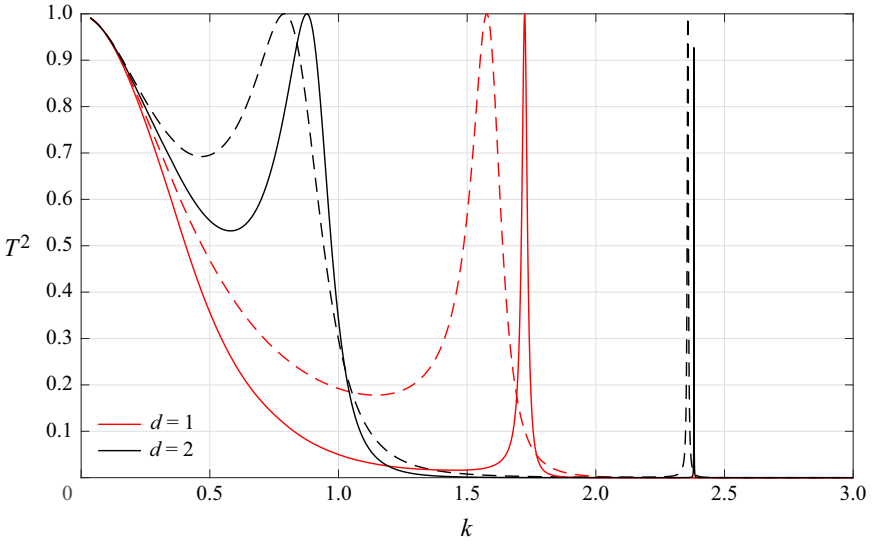

Figure 6. Transmission coefficient as a function of the wavenumber k at fixed distances d and $L = 1$. The dashed lines represent particular solution and general solution for the case of $N = 1$. Solid lines show general solution with $N = 32$.

as shown in figure 8. The larger the distance between the barriers, the larger the variance about the peaks becomes. This suggests a possible non-dimensional number that governs the physical problem.

Notably, the general solution, consisting of a progressive mode before the barrier(s) and an evanescent mode over the bump region(s), aligns with the particular solution derived in §§ 3.1 and 4.1. This solution is equivalent to the one commonly discussed in the quantum

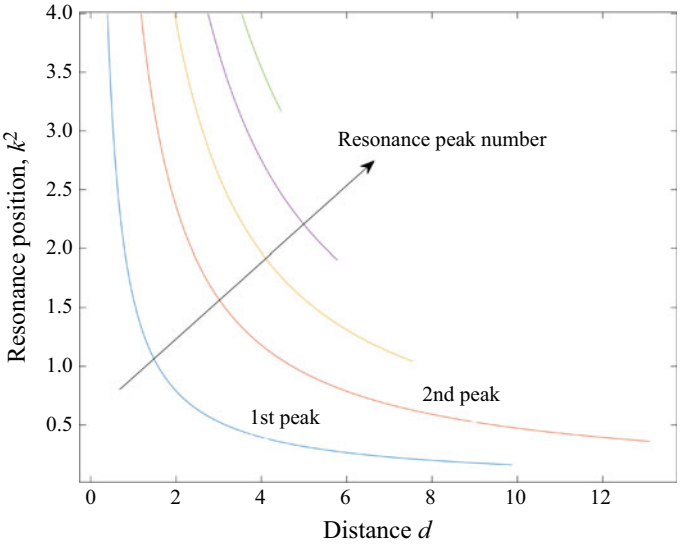

Figure 7. Peaks of transmitted energy (resonance) as a function of the inter-barrier distance d for the case of symmetric double barriers.

tunnelling literature (e.g. Strekalov (2018)) Due to this consistency, we adopted the general solution for generating the plots presented in this work in figures 3–6.

4.2. *Energy transformation between modes*

This section examines the interaction of multiple modes with a single barrier, as the modes transition from evanescent to progressive states due to varying barrier heights. It is found that energy distribution between modes after the barrier is highly dependent on the incident mode and the barrier height (potential). Moreover, a significant mode switching is observed near the critical heights where modes change from evanescent to progressive, and energy essentially transforms between the modes.

To gain a more quantitative understanding of this energy transformation we consider a numerical example (figure 9) comprising three progressive modes allowed in region (0) where $\lambda = 0.75 \times z_0^{(0)}$. The general solution presented in § 3 is truncated for a total of ten modes, including both progressive and evanescent types, to ensure accuracy (e.g. see Kadri & Stiassnie 2012). The figure illustrates the transmission coefficient T^2 as a function of the normalised barrier length and height (potential). The columns correspond to the number of the incident mode, whereas the rows depict the transmission coefficient in a specific mode number. For example, panel (c) corresponds to the transmission coefficient in mode 3 provided that mode 1 is the incident mode; whereas panel (h) corresponds to the transmission coefficient in mode 2 after an incident mode 3. In each panel, the horizontal solid, dashed and dotted white lines indicate the critical potential at which modes 1, 2 and 3 transition from evanescent to progressive states, respectively.

Panel (a) shows the expected behaviour where, as the potential increases, the transmitted energy remains in the same mode. However, due to the existence of higher progressive modes, once the barrier potential allows it (as seen in panel b), the energy is shared between modes 1 and 2. Tunnelling still occurs, and the amount of energy in mode 1 is larger than in mode 2, but once permitted, some energy leaks to mode 2. A small portion of energy also transfers to mode 3, as shown in panel (c). This mode-switching behaviour contrasts with the previous section, where only one progressive mode was

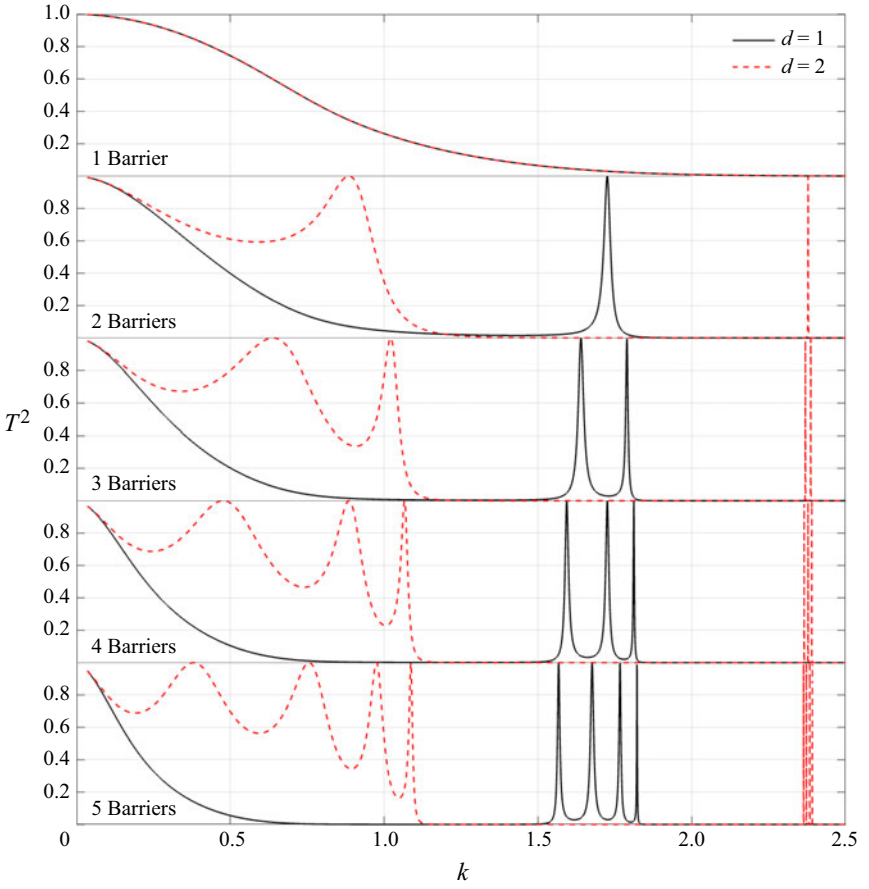

Figure 8. Transmission coefficient as a function of the wavenumber k at fixed distances $d = 1,\ 2$ and $L = 1$ for 1–5 barriers calculated by the general solution with $N = 32$.

allowed, resulting in energy transferring to the next lowest neighbouring mode – in this case from mode 1 to mode 2 – near the critical potential (cutoff depth).

When the incident mode is not the lowest, as in the middle column (panels d,e,f), where the second mode is the incident ($\hat{i} = 2$), energy distributes almost equally between modes 1 and 2 near the dashed line corresponding to the critical potential of mode 2. As the barrier potential decreases and approaches the point where mode 3 turns progressive, energy begins to transfer to the third mode as well (panel f).

In the case where mode 3 is the incident ($\hat{i} = 3$), i.e. right column with panels g,h,i, only the first mode is progressive in region (1), for large barrier potentials (below the solid line), almost one third of the transmitted energy transfers to modes 1 and 2. In panel (h), as the barrier potential decreases beyond the dashed line, energy begins to split between modes 2 and 3. Finally, when all modes are progressive (below the dotted line), energy predominantly remains in the third mode, as shown in panel (i).

It is worth noting that resonances due to the barrier length may result in a more efficient energy transfer between modes. For example, when the incident mode is $\hat{i} = 1$ more than 16 % of the energy may transfer to the next lowest mode 2 (panel b), although at a specific range of barrier lengths a similar percentage (approximately 12 %) is transferred to mode 3

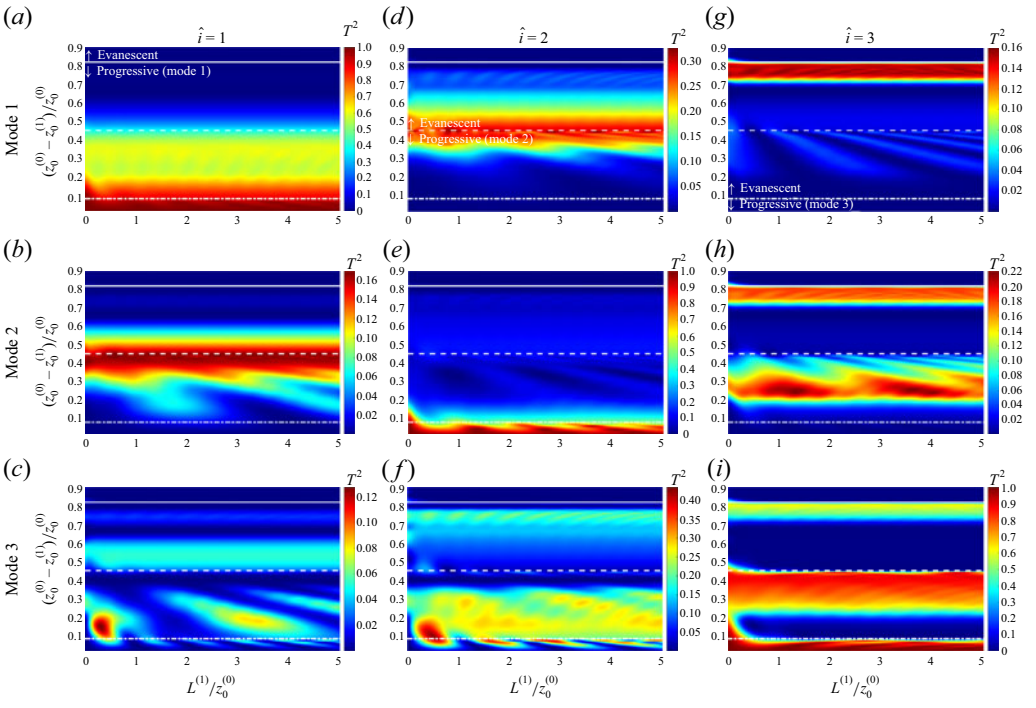

Figure 9. Effects of barrier length and potential on the transmission coefficient for: mode 1 (*a*,*d*,*g*); mode 2 (*b*,*e*,*h*); mode 3 (*c*,*f*,*i*) for three progressive incident modes in region (0): $\hat{i}=1$ (*a*,*b*,*c*); $\hat{i}=2$ (*d*,*e*,*f*); $\hat{i}=3$ (*g*,*h*,*i*). The corresponding barrier potential to progressive and evanescent mode limits are shown by horizontal white lines. In all computations a total of 32 modes (up to 3 progressive) were considered.

(panel *c*). When the incident mode is $\hat{i}=2$ almost 40 % of the energy can transfer to mode 3 provided the optimal barrier length is employed (panel *f*).

4.3. *A note on Anderson localisation: multi-barrier disorder*

Anderson localisation is a phenomenon in condensed matter physics where the wave-like properties of particles (such as electrons in a disordered medium) become localised and cannot propagate through the material. This was first proposed by physicist Philip W. Anderson in 1958, who showed that, in a sufficiently disordered lattice (random arrangement of atoms or molecules), the interference of scattered waves can lead to a complete halt in particle transport Anderson (1958).

In practical terms, Anderson localisation explains why electrons in disordered materials (like amorphous solids or doped semiconductors) can become trapped, leading to insulating behaviour even in materials that might otherwise conduct electricity. A similar behaviour is observed, when considering an incident acoustic-gravity wave interacting with multi-barriers (§ 4). As is shown in figure 10, the transmission was evaluated for 1000 randomly generated instances, each with variations in barrier height and width disturbances, where $|\Delta z_0^{(b)}| \leqslant 1/2$ and $|\Delta L^{(b)}| \leqslant 1/2$. The disorder parameter is characterised by the diagonal length, given by $\sqrt{\{\Delta z_0^{(b)}\}^2+\{\Delta L^{(b)}\}^2}$. The domain length is set to 100; the average barrier height $\overline{z_0^{(b)}}=0.85$; and the average barrier length $\overline{L^{(b)}}=2$. The incident wavelength is $\lambda=4$, where full transmission occurs under the condition $\Delta z_0^{(b)}=\Delta L^{(b)}=0$.

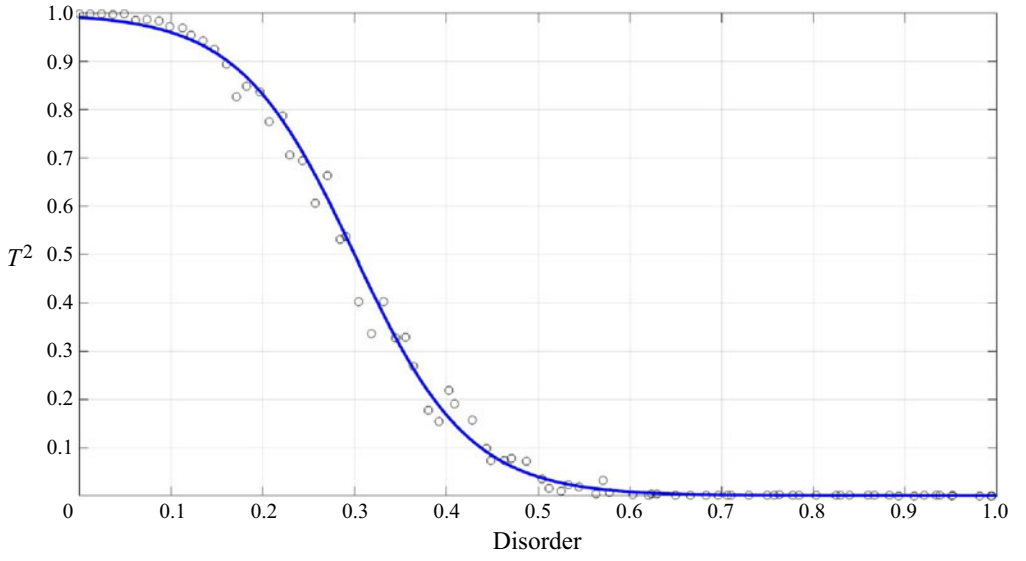

Figure 10. Effect of barrier disorder (Anderson localisation) on the transmission coefficient.

4.3.1. *Implication to the Argentinian ARA San Juan submarine*

The ARA San Juan, a TR-1700-class submarine of the Argentine Navy, sank on 15 November 2017 during a routine patrol in the South Atlantic, resulting in the loss of all 44 crew members. Shortly after the submarine reported a battery fire, acoustic signals consistent with an implosion was recorded by hydroacoustic stations of the Comprehensive Nuclear-Test-Ban Treaty Organisation (CTBTO), Ascension (H10) and Crozet Islands (H04) (Vergoz *et al.* 2021), as well as at Juan Fernandez Island hydroacoustic station (H03S) (Kadri 2024). The recorded signals played a critical role in narrowing the search area, leading to the discovery of the wreckage a year later, in November 2018, at a depth exceeding 900 m.

Vergoz *et al.* (2021) carried out a comprehensive analysis on the acoustic signals associated with the submarine incident. As shown in figure 11, the submarine was last located at 45.950°S, 59.773°W, approximately 6300 km from the H10N hydrophone, positioned at 7.840°S, 14.480°W. The acoustic waves generated by the event predominantly fall within the frequency range of 7–10 Hz Vergoz *et al.* (2021). These waves are trapped in the sound fixing and ranging (SOFAR) channel, enabling their propagation over long distances with minimal attenuation. However, the Rio Grande Seamount lies between the incident location and the hydrophone. Notably, the seamount's summit intersects the SOFAR channel depth, which is approximately 2000 m below the ocean surface. This interaction likely disrupts the acoustic waves' propagation within the SOFAR channel, causing energy dissipation and scattering.

To analyse this interference, we modelled the region where the Rio Grande Seamount and the lower boundary of the SOFAR channel intersect, spanning an effective length of approximately 250 km. Based on the geometry shown in panel (*b*) of figure 11, we considered the average depth of seamount bumps within the highlighted area to be around 60 % of the SOFAR channel's depth. Using this configuration, we investigated the transmission coefficient for acoustic waves in the 7–10 Hz frequency range under a multi-bump scenario with random bottom topography.

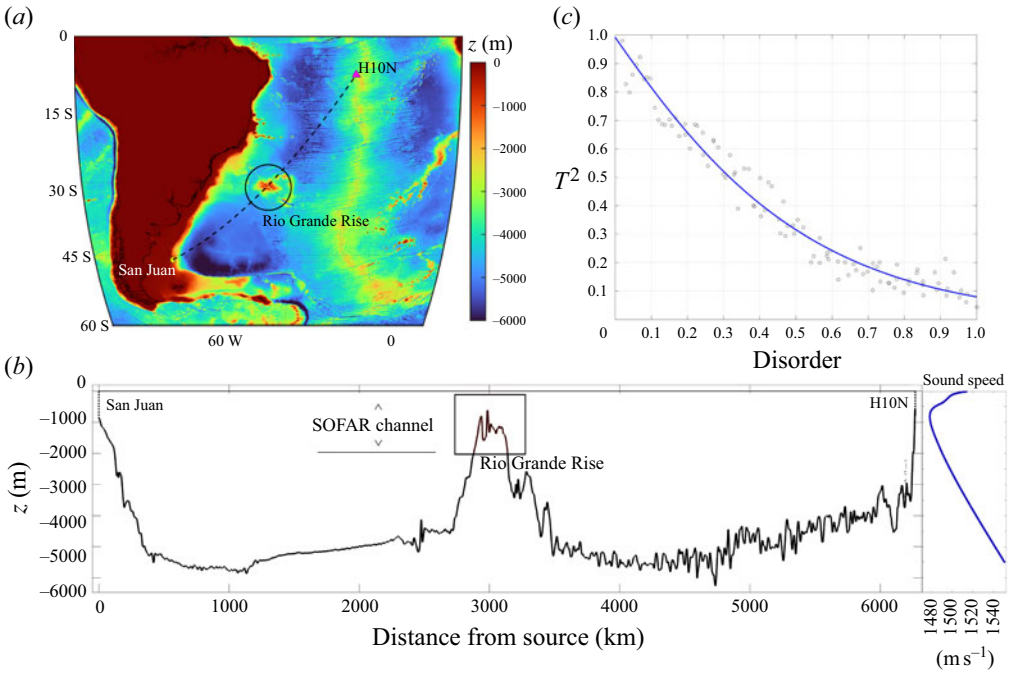

Figure 11. (*a*) Bathymetric map of the eastern coast of South America, showing the location of the San Juan submarine disappearance on 17 November 2017, the H10N hydrophone coordinates and the connecting path across the Rio Grande Rise; (*b*) vertical transect along the connecting path, displaying sound speed profiles and the estimated SOFAR channel, corresponding to the minimum temperature layers. A highlighted box indicates the region where acoustic signals interact with the seamount; (*c*) effect of barrier disorder on the transmission coefficient for waves with frequencies ranging from 7 to 10 Hz, passing through multi-bump barriers with a total length of 250 km and an average blockage of 60 %.

The level of disorder (panel *c*) quantifies the randomness in the multi-barrier configurations, characterised by variations in barrier length and height. A disorder value close to 0 indicates minimal deviation from the mean values, while a disorder value of 1 corresponds to the maximum degree of randomness in the configuration. The transmission coefficient was evaluated across 1000 randomly generated instances (figure 11). Each instance featured variations in barrier height and width, constrained by $|\Delta z_0^{(b)}| \leqslant 0.5$ and $|\Delta L^{(b)}| \leqslant 1$, respectively. The average barrier height and length were set at $\overline{z_0^{(b)}} = 0.6$ and $\overline{L^{(b)}} = 10$, respectively. This statistical approach enabled us to assess the impact of random seafloor configurations on wave transmission within the specified frequency range.

5. Concluding remarks

Motivated by quantum tunnelling phenomena, we studied the interaction of acoustic-gravity waves with rectangular barriers. The analytical solution for transmission (and reflection) coefficients in the case of a single barrier is found to be analogue to quantum tunnelling, where the transmission decays exponentially with increasing barrier width (assuming a single mode in each region). For the double-barrier case, resonance conditions allow full transmission through tunnelling, again analogously to quantum tunnelling (Strekalov 2018).

Moreover, we derived a general multi-barrier solution that allows the propagation of many modes at any given configuration of barriers. The general solution is interesting from two different perspectives. Firstly, it suggests that acoustic-gravity waves can transmit energy even beyond a turning point, e.g. due to shoaling, or due to bathymetric barriers. This could have implications for short signals travelling large distances, through bathymetric barriers as in the case of the Argentinian ARA San Juan Submarine.

It is crucial to emphasise that accounting for the elasticity of the sea floor, a necessary consideration in shallow water and near-critical depth scenarios, fundamentally alters wave propagation. Under these conditions, only the leading mode propagates through the elastic medium (Eyov *et al.* 2013), significantly reducing reflection and enhancing transmission efficiency – unless tunnelling from only higher acoustic modes is considered – deviating from the classical analogy with quantum tunnelling. However, even when the leading acoustic-gravity mode couples with the elastic sea floor, the problem can be conceptually divided into two parts: penetration through the elastic barrier and tunnelling. The solution to the first part is essentially provided in (3.1), with $\sin(\kappa L)$ replacing $\sinh(\kappa L)$, as is well established in the literature (see Brekhovskikh 1980, pp. 23–26). The solution to the second part, while conceptually similar to the one provided here, becomes dynamically more complex due to increased phase speed and greater energy transfer to the surface-gravity mode, which can no longer be neglected in shallow-water scenarios. This insight not only offers a new perspective on the wave dynamics in elastic media but also highlights the significant role of the surface-gravity mode in shallow water tunnelling phenomena. Further exploration of the gravity mode's effects under such conditions represents an essential step towards a more comprehensive understanding of wave–sea floor interactions, with potential implications for both geophysics and quantum analogue systems.

Declaration of interests. The authors report no conflict of interest.

References

Abdolali, A., Kadri, U. & Kirby, J.T. 2019 Effect of water compressibility, sea-floor elasticity, and field gravitational potential on tsunami phase speed. *Sci. Rep.* **8**, 16874.

Abdolali, A., Kirby, J.T. & Bellotti, G. 2015 Depth-integrated equation for hydro-acoustic waves with bottom damping. *J. Fluid Mech.* **766**, R1.

Anderson, P.W. 1958 Absence of diffusion in certain random lattices. *Phys. Rev.* **109**, 1492–1505.

Balantekin, A.B. & Takigawa, N. 1998 Quantum tunneling in nuclear fusion. *Rev. Mod. Phys.* **70**, 77–100.

Bondi, H. 1947 Waves on the surface of a compressible liquid. *Math. Proc. Cambridge Phil. Soc.* **43** (1), 75–95.

Brekhovskikh, L.M. 1980 *Waves in Layered Media*. 2nd edn. Academic Press.

Child, M.S. 1967 Measurable consequences of a dip in the activation barrier for an adiabatic chemical reaction. *Mol. Phys.* **12** (5), 401–416.

Connor, J.N.L. 1968 On the analytical description of resonance tunnelling reactions. *Mol. Phys.* **15** (1), 37–46.

Eyov, E., Klar, A., Kadri, U. & Stiassnie, M. 2013 Progressive waves in a compressible-ocean with an elastic bottom. *Wave Motion* **50** (5), 929–939.

Kadri, U. 2015 Acoustic-gravity waves interacting with a rectangular trench. *Intl J. Geophys.* **2015**, 806834.

Kadri, U. 2024 Underwater acoustic analysis reveals unique pressure signals associated with aircraft crashes in the sea: revisiting MH370. *Sci. Rep.* **14**, 10102.

Kadri, U. & Stiassnie, M. 2012 Acoustic-gravity waves interacting with the shelf break. *J. Geophys. Res.* **117**, C03035.

Kelly, M.J. & Weisbuch, C. 1986 *The Physics and Fabrication of Microstructures and Microdevices*. Springer Proceedings in Physics.

Kirby, J.T. & Dalrymple, R.A. 1983 Propagation of obliquely incident water waves over a trench. *J. Fluid Mech.* **133**, 47–63.

MEI, C.C., STIASSNIE, M.A. & YUE, D.K.-P. 2005 *Theory and Applications of Ocean Surface Waves: Part 1: Linear Aspects*. World Scientific.

MICHELE, S. & RENZI, E. 2020 Effects of the sound speed vertical profile on the evolution of hydroacoustic waves. *J. Fluid Mech.* **883**, A28.

SAMMARCO, P., CECIONI, C., BELLOTTI, G. & ABDOLALI, A. 2013 Depth-integrated equation for large-scale modelling of low-frequency hydroacoustic waves. *J. Fluid Mech.* **722**, R6.

STREKALOV, M.L. 2018 Quantum tunneling in an exactly solvable double-barrier potential: barrier transmission near the zero energy. *J. Math. Chem.* **56**, 890–903.

THOMSON, J., ELGAR, S. & HERBERS, T.H.C. 2005 Reflection and tunneling of ocean waves observed at a submarine canyon. *Geophys. Res. Lett.* **32**, L10602.

VERGOZ, J., CANSI, Y., CANO, Y.& GAILLARD, P. 2021 Analysis of hydroacoustic signals associated to the loss of the Argentinian ARA San Juan submarine. *Pure Appl. Geophys.* **178** (7), 2527–2556.

ZUCCOLI, E. & KADRI, U. 2025 Resonant triad interactions of two acoustic modes and a gravity wave. *J. Fluid Mech.* **1008**, A15.